White Rose Research Online
eprints@whiterose.ac.uk
https://eprints.whiterose.ac.uk
Universities of Leeds, Sheffield and York

Deposited via The University of Sheffield.

White Rose Research Online URL for this paper:
https://eprints.whiterose.ac.uk/id/eprint/240982/

Version: Published Version

Article:

Bowe, D.A., Ford, K.L. and Tennant, A. (2026) Adapting mixer metamaterials with a metasurface absorber. IET Radar, Sonar & Navigation, 20 (1). e70150. ISSN: 1751-8784

https://doi.org/10.1049/rsn2.70150

Reuse

This article is distributed under the terms of the Creative Commons Attribution (CC BY) licence. This licence allows you to distribute, remix, tweak, and build upon the work, even commercially, as long as you credit the authors for the original work. More information and the full terms of the licence here: https://creativecommons.org/licenses/

Takedown

If you consider content in White Rose Research Online to be in breach of UK law, please notify us by emailing eprints@whiterose.ac.uk including the URL of the record and the reason for the withdrawal request.

UNIVERSITY OF LEEDS
University of Sheffield
UNIVERSITY of York

IET Radar, Sonar & Navigation

WILEY

The Institution of Engineering and Technology

ORIGINAL RESEARCH OPEN ACCESS

Adapting Mixer Metamaterials With a Metasurface Absorber

Douglas A. Bowe | Kenneth L. Ford | Alan Tennant

School of Electrical and Electronic Engineering, University of Sheffield, Sheffield, UK

Correspondence: Kenneth L. Ford (l.ford@sheffield.ac.uk)

Received: 12 December 2025 | **Revised:** 30 March 2026 | **Accepted:** 8 April 2026

Keywords: absorbers | frequency selective surfaces | mixers (circuits)

ABSTRACT

This paper presents an in-depth study of mixer metasurfaces comprising a frequency-selective surface (FSS) mixer layer and a secondary transmission line local oscillator (LO) layer. Through both simulation and experimental measurement, we demonstrate how an upconverted signal is maximised by optimising metamaterial design and the separation of mixer components. Local oscillator signals at 2.1, 3, 4.2, and 4.45GHz were applied to the LO layer to drive the switching diodes on the mixer layer. The resulting metamaterial reflectivity, transmission, surface currents, scattering patterns, and 1D probe data were analysed, with results from a large-scale fabricated model verifying the simulations. Finally, the structure is augmented with a metamaterial absorber to suppress generated harmonics, demonstrating a novel multi-layered approach to incident signal manipulation and scattering control.

1 | Introduction

Controlling and reducing electromagnetic (EM) scattering of signals is an area of significant interest across various sectors, such as within the aviation and maritime industries [1, 2]. Although this interest has driven the development of numerous design methodologies, approaches such as mixer diodes have only seen limited use. Although basic semiconductor components have been used before for resistive tuning [3], this work aims to expand and establish a new concept for mixer-based metamaterials.

In metamaterial research, various types of transmitting surfaces have been designed using nonlinear devices to introduce effects such as variable resistance, capacitance and signal mixing, documented from the 1990s to the present day [4–8]. Metamaterials represent a broad research field valued for their unique properties, with frequency-selective surfaces (FSSs) functioning as low-pass, high-pass, bandpass or bandstop filters as well as absorbers [9–11]. These properties arise from the inductive and capacitive effects of geometric patterns printed on a substrate, which enable passive filtration properties. Electronic components can further enhance the inductive or capacitive characteristics of a metamaterial. Components such as PIN and mixer diodes that contribute to resistive and mixing effects can also introduce parasitic capacitance and inductance. These properties can shift the operating frequency of the structure and have been used for tuning applications [12–14].

In the context of mixing, various electromagnetic and metamaterial structures, such as diode grid mixers, have been developed to utilise the superheterodyne effect for combining two signals. When an AC stimulus is applied, it activates the diodes, generating the desired $f_1 \pm f_2$ harmonics. Mixer-based metamaterials have previously been employed to achieve this effect by combining two signals that illuminate metamaterial structures, and a DC biasing signal switches on the diodes to the desired nonlinear region [15–17]. These metamaterials have been designed by adapting research taken from the literature [18, 19] and adding Schottky diodes to the surface. This creates

This is an open access article under the terms of the Creative Commons Attribution License, which permits use, distribution and reproduction in any medium, provided the original work is properly cited.

© 2026 The Author(s). *IET Radar, Sonar & Navigation* published by John Wiley & Sons Ltd on behalf of The Institution of Engineering and Technology.

multiple-element, single- and multidiode grid mixers that have been capable of drawing a downconverted signal from the mixer diodes to a ground point or off a surface [16, 17]. The superheterodyne principle has also been applied in harmonic tags for wildlife and object tracking, where minimal RF circuitry and mixer components facilitate frequency doubling [20, 21].

This study advances previous work [22] by transitioning from a 4×4 metamaterial mixer structure to a larger 8×8 array with an expanded LO layer. The 8×8 configuration is used to mitigate edge effects, whereas the expanded LO layer provides an AC stimulus necessary to bias the diodes. This enables the mixing of an LO signal (f_{LO}) with an incident signal (f_i) allowing for a more comprehensive analysis than previously possible. For demonstration, a target 6.2-GHz signal is generated by illuminating the structure with a 2-GHz incident wave, whereas a 4.2-GHz signal is fed through the LO layer. Although the response of metamaterials across various frequencies is well documented, the specific frequency range selected for this paper was determined by the availability of silicon-based components and the requirement for design simplicity.

Metamaterial absorbers are designed to suppress specific frequencies based on their structural design, a capability utilised to modify the radar cross-section (RCS) of dipole antennas [23] and control the scattering of phased arrays [24–26]. Building on these techniques, this study proposes that, by integrating an absorber with a metamaterial capable of frequency upconversion, the resulting harmonics can be effectively dissipated. This multilayered approach introduces a novel method for scattering control, whereby an incident signal is upconverted by a mixer layer and subsequently captured by an absorbing layer. Because these target harmonics exist at higher frequencies, the required absorbing structure can be significantly thinner than conventional low-frequency counterparts.

Within the scope of this research, simulations and measurements are conducted to model and verify the mixer effect within these metamaterial structures. These findings provide a foundation for future designs, offering a framework to optimise or augment mixer-based metamaterials. Potential applications include the development of dual-band metamaterials, the mixing of multiple input signals and the exploration of novel avenues in metamaterial research. Furthermore, this approach enables the miniaturisation of future absorber designs by integrating common metamaterial architectures with active mixer components.

2 | Model Design and Structure Configuration

2.1 | Structure Configuration

Figure 1a shows the basic concept of the multilayered superheterodyne metamaterial; this structure consists of an FSS layer with silicon oxide Schottky diodes that make the surface act as a mixer layer when excited by an external stimulus. A local oscillator (LO) layer is positioned 3 mm beneath the mixer layer to provide an AC stimulus via a transmission line network. For demonstration purposes, this network is optimised to minimise losses at 4.2 GHz. When an external LO signal is applied, the mixer layer upconverts a 2-GHz incident signal to 6.2 GHz, which is then re-radiated. This upconversion mechanism reduces the magnitude of the original incident signal. Furthermore, the mixing efficiency can be modulated by adjusting the LO signal magnitude, thereby controlling the interaction across the Schottky diodes.

The 3-mm separation between layers was maintained in both simulation and measurement to ensure effective LO signal coupling while minimising parasitic losses and structural reflectivity. Finally, as depicted in Figure 1b, an absorber layer is integrated into the structure to suppress unwanted harmonics and further attenuate the illuminating signal.

2.2 | Mixer Layer Unit-Cell Design

A mixer layer unit cell consists of a single aperture loop printed on a 1-mm-thick FR-4 substrate with a single central patch FSS and is used for the bandwidth it provides at the target frequency (2 GHz ± 200 MHz), using the same design as in Ref. [22]. To achieve the mixing effect, two Schottky diode pairs are connected across the gap in the loop, as illustrated in Figure 2. The design parameters in Table 1 are implemented to ensure resonance at 2 GHz. The aperture loop design was selected for its

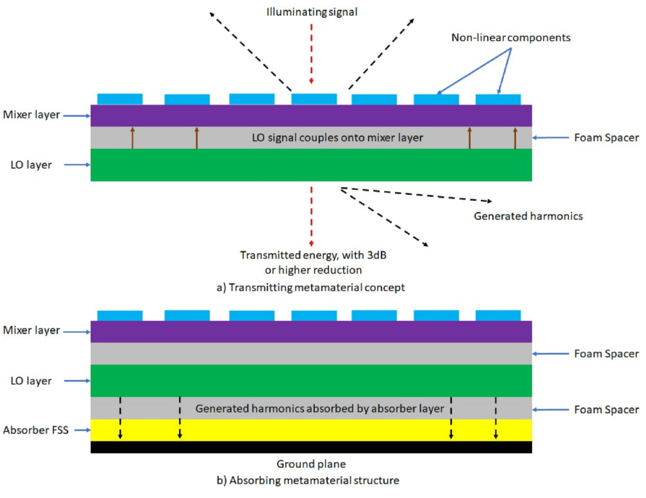

FIGURE 1 | Diagrams of transmitting metamaterial and full absorber structures.

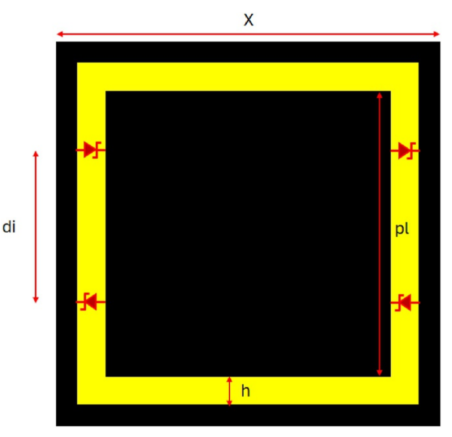

FIGURE 2 | Mixer layer unit cell with PEC denoted in black and FR-4 in yellow.

17518792, 2026, 1, Downloaded from https://ietresearch.onlinelibrary.wiley.com/doi/10.1049/rsn2.70150 by NICE, National Institute for Health and Care Excellence, Wiley Online Library on [11/05/2026]. See the Terms and Conditions (https://onlinelibrary.wiley.com/terms-and-conditions) on Wiley Online Library for rules of use; OA articles are governed by the applicable Creative Commons License

structural simplicity and the ease with which diodes can be integrated into the surface for mixing. Although alternative components such as transistors or integrated circuit (IC) mixers could be considered, they introduce significant architectural complexity. Incorporating such components into a square aperture loop would necessitate extensive redesigns. Furthermore, the additional interconnects required for active mixers could adversely affect the frequency response.

The structure is designed to resonate at 2 GHz, utilising diode pairs to provide the mixing required for upconversion. Although downconversion is possible using this approach, it is limited by the FSS unit-cell size and is beyond the scope of this study.

2.3 | LO Layer Unit-Cell Design

The LO layer consists of a transmission line network configured to minimise losses at a single frequency. The design of this layer follows the concept in Figure 3, whereby a parallel, separated microstrip is adopted. Using this topology, we can vary the line separation, substrate thickness and width of the two lines, thereby controlling the characteristic impedance. Furthermore, the electric field distribution (indicated by red dotted lines in Figure 4) may be induced using an LO signal connected between the (+) and (−) conductors. These conductors are shown in Figure 3 as the black and grey lines that denote the parallel lines on either side of a 1.2-mm-thick FR-4 substrate. These fields are polarised to maximise induced currents on the mixer layer. These currents flow through the diodes, providing both the required stimulus and the f_{LO} signal necessary to upconvert the incident signal (f_i). To minimise reflections, the LO layer can be extended and connected to a specifically designed frequency splitter. The LO layer shown in Figure 3 is designed according to the parameters in Table 2 to achieve a characteristic impedance of 100 Ω, ensuring compatibility with the splitter depicted in Figure 5. This transmission line splitter is designed using the parameters in Table 3, whereby the input is matched to an input impedance of 50Ω and by using a T-split power divider topology [27], the output lines of the splitter have a characteristic impedance of 100Ω, such that it can connect to the parallel separated transmission lines with minimal reflections. This process may be repeated multiple times depending on the available power levels and the desired size of the LO layer.

TABLE 1 | Mixer layer design parameters.

Parameter	*X*	di	pl	*h*
Value/mm	39.8	26	28.8	2

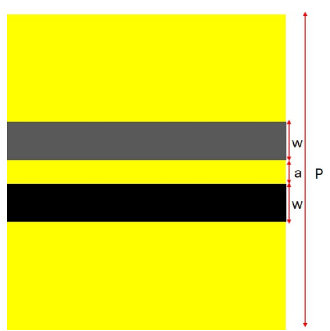

FIGURE 3 | Unit-cell LO layer.

A larger, complete architecture can be realised by integrating two sets of transmission line splitters. These are matched to 50 Ω at the inputs, with outputs feeding directly into the LO layer. To achieve the required 100 Ω output impedance and ensure compatibility with the previously designed differential lines, the microstrip traces are physically separated at the splitter outputs. Furthermore, the lines feature chamfered and mitred bends to optimise the overall S-parameter response. These design refinements minimise reflections at the interface with the primary transmission line situated beneath the mixer layer.

2.4 | Absorber Layer Concept

As illustrated in Figure 1b, an absorber layer is integrated to dissipate the upconverted harmonics scattered into the far field. For this design, a Salisbury screen metasurface absorber is selected due to its structural simplicity. The absorber comprises a dual-polarised FSS situated above a ground plane, utilising the same aperture loop concept as the mixer layer. Surface-mount resistors connect the outer loop to the inner patch to provide the necessary resistance for matching the free-space impedance, η_0 (377 Ω). When the optimal separation distance *D* between the ground plane and the FSS is established, the structure achieves

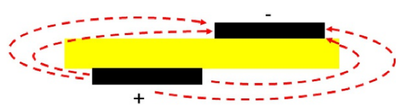

FIGURE 4 | Transmission line concept.

TABLE 2 | LO layer design parameters.

Parameter	*P*	*a*	*w*
Value/mm	39.8	26	4.2

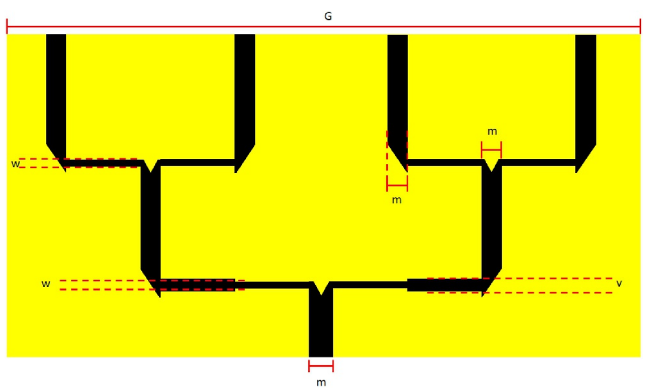

FIGURE 5 | LO layer splitter network that connects to LO layer.

TABLE 3 | Splitter design parameters.

Parameter	*G*	*m*	*v*	*w*
Value/mm	159.2	3.2	1.1	4.2

17518792, 2026, 1, Downloaded from https://ietresearch.onlinelibrary.wiley.com/doi/10.1049/rsn2.70150 by NICE, National Institute for Health and Care Excellence, Wiley Online Library on [11/05/2026]. See the Terms and Conditions (https://onlinelibrary.wiley.com/terms-and-conditions) on Wiley Online Library for rules of use; OA articles are governed by the applicable Creative Commons License

minimal reflectivity at 6.2 GHz. This configuration effectively suppresses unwanted harmonics without interfering with the primary mixing operation. In this work, the FSS Salisbury screen depicted in Figure 6 with parameters detailed in Table 4 serves as a proof of concept for the integrated mixer-absorber architecture.

3 | Simulation

3.1 | Simulation of Individual Layers

Preliminary simulations of the two individual layers in Figures 2 and 3 were carried out to find the transmitting frequency and S-parameters of the two layers, respectively. The results in Figure 7 show the simulated reflectivity and transmission, where the mixer layer displays a resonant reflectivity at 2.05 GHz with a magnitude of −31 dB and behaves as a transmitting surface at this frequency. Although the targeted frequency was 2 GHz, the design choice was intentionally offset to compensate for the frequency shift expected when integrated with the LO layer. The coupling between the input and ground lines is illustrated in Figure 8, where the electric field orientation is optimised to induce diode currents once the mixer layer is positioned above. Simulation data indicate that increasing the separation between layers significantly reduces the induced current, as the electric field amplitude decays rapidly with distance. This attenuation is visualised in the vector plot, where field magnitudes decrease from 34, 613 V/m at the source to less than 400 V/m as the distance increases.

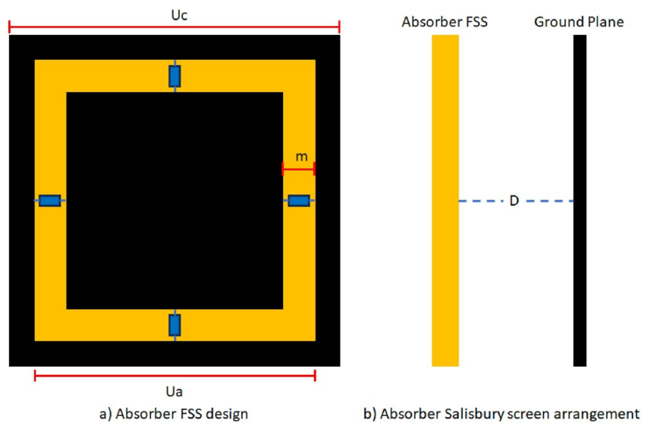

FIGURE 6 | Absorber layer unit cell with PEC denoted in black and FR-4 in yellow.

TABLE 4 | Absorber layer design parameters.

Parameter	Uc	Ua	*g*	*D*
Value/mm	19.9	16.82	2	21

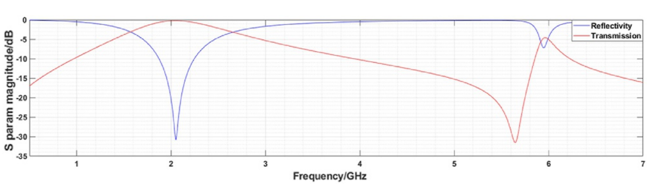

FIGURE 7 | Reflectivity and transmission results of mixer layer alone.

Figures 9 and 10 present the simulated S-parameters for the integrated LO architecture, including all splitters and transmission lines. As expected, the complexity of the combined structure leads to a marginal increase in both insertion loss and reflections. The S_{11} results remain below -20 dB at 4.2 GHz, indicating excellent impedance matching at the input. Although the S_{21} magnitude is slightly higher than anticipated, remaining just above -10 dB at 4.2 GHz, this is primarily attributed to the physical length of the LO distribution network. For this proof-of-concept demonstration, these performance metrics are acceptable; however, future iterations could be optimised to further reduce ohmic losses and enhance coupling efficiency.

3.2 | Mixing and Optimisation of Signals

When determining the optimal diode placement, three topologies were evaluated based on their current distributions at the 6.2-GHz harmonic frequency, as shown in Figure 11. Analysing the direction and magnitude of these currents is essential, as

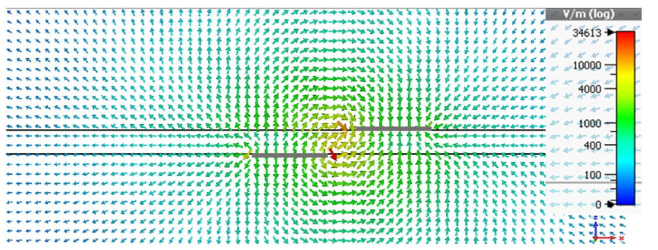

FIGURE 8 | E-fields round the LO layer.

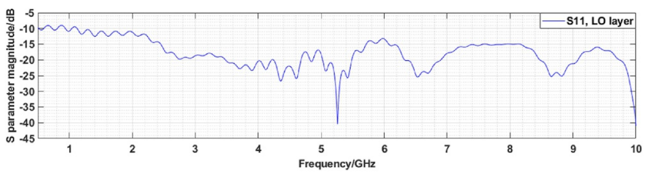

FIGURE 9 | S11 result of LO layer when splitters are connected to microstrip.

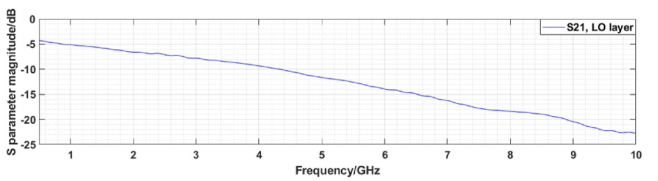

FIGURE 10 | S21 result of LO layer when splitters are connected to microstrip.

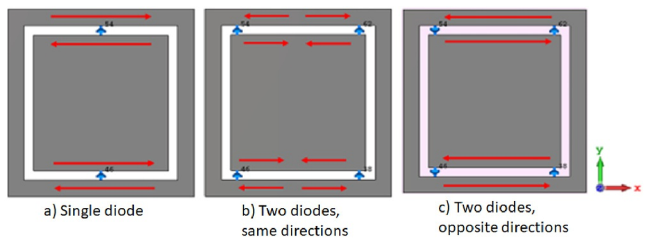

FIGURE 11 | Current distribution for different diode orientations.

17518792, 2026, 1, Downloaded from https://ietresearch.onlinelibrary.wiley.com/doi/10.1049/rsn2.70150 by NICE, National Institute for Health and Care Excellence, Wiley Online Library on [11/05/2026]. See the Terms and Conditions (https://onlinelibrary.wiley.com/terms-and-conditions) on Wiley Online Library for rules of use; OA articles are governed by the applicable Creative Commons License

they directly dictate the radiation characteristics of the generated harmonics.

In the single-diode arrangement in Figure 11a, currents on opposite sides of the aperture loop flow in opposing directions. Specifically, the single-diode results in a phase mismatch across the gap, preventing a coherent radiating mode. To resolve this, dual-diode configurations were investigated to establish a circulating current loop.

In the configuration shown in Figure 11b, although two diodes are used, their identical orientation prevents the formation of a continuous loop. Instead, the currents flow in opposing directions, leading to destructive interference that significantly degrades harmonic radiation. This led to the final design (Figure 11c), where the diodes in each pair are oriented in opposite directions (antiparallel). This arrangement facilitates a circulating current path between the diodes, effectively forming a current loop that radiates the harmonic more efficiently than the previous iterations.

To optimise the magnitude of the harmonics, a preliminary study was conducted to determine how diode placement influences surface current distribution, as shown in Figure 12. We compared the surface currents generated for 5 and 6.2 GHz outputs, resulting from 3 to 4.2 GHz LO signals, respectively. The results reveal current loops circulating between the two diode pairs, effectively forming a radiating element within the aperture loop. With a fixed diode separation of 26 mm, the spacing approaches $\lambda/2$ for the 6.2-GHz harmonic ($\lambda = 48$ mm), but not for the 5-GHz signal ($\lambda = 60$ mm). This $\lambda/2$ separation facilitates optimal radiation of the 6.2-GHz harmonic, as evidenced by the enhanced resonance effects shown in Figure 12a,b. This behaviour compares well with previous research where lumped reactive components were utilised to induce similar resonant effects [28]. This resonance is further validated by the normalised E-field spectra in Figure 13. When the LO frequency is 3 GHz, the resulting 5-GHz harmonic is 10 dB lower than the 6.2-GHz harmonic produced by a 4.2-GHz LO signal (normalised amplitudes of -19.3 dB and -9.6 dB, respectively). Although frequency-dependent scattering may contribute to this discrepancy, it cannot account for the full 10-dB difference; the increased amplitude is primarily attributed to the optimised surface current distribution at 6.2 GHz. Furthermore, the LO signal amplitude significantly influences the mixer's operating state. We observed that the 4.2-GHz LO signal reaches a higher normalised amplitude (11.9 dB) compared to the 3-GHz signal (-1.4 dB), likely due to antenna gain effects

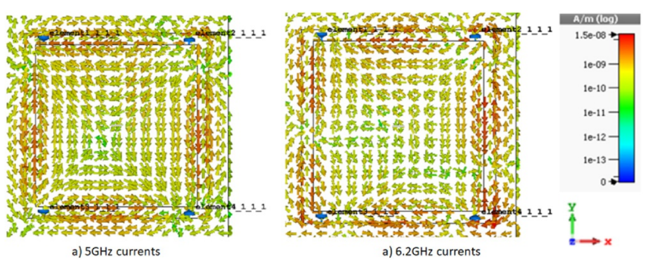

FIGURE 12 | Current distribution around the aperture loop when LO power is 14 dBm.

within the LO layer. This variation in LO magnitude affects diode saturation levels, which, in turn, modulates the suppression of the 2-GHz incident signal. Specifically, the 2-GHz signal is reduced to -3.3 dBV/m when using a 3-GHz LO, whereas it remains at 0 dB with an LO frequency of 4.2 GHz, indicating that the mixing efficiency is highly dependent on the LO power level.

A parametric study was conducted to evaluate the impact of diode separation (*di* in Figure 2) by varying the distance from 6 to 26 mm (Figure 14). As illustrated in Figure 14a, the magnitude of the 2-GHz incident signal decreased as the diode separation was increased in 4 mm increments. This provided a tuning range from -0.9 dB at a 6-mm separation to -4.9 dB at 26 mm. Conversely, Figure 14b demonstrates that the desired 6.2-GHz harmonic reached its peak magnitude of -4.2 dB at a separation of 26 mm, approximately $\lambda/2$ before dropping to -8.6 dB at 18 mm. These findings justify the selection of the 26-mm separation for the final design, as it maximises the 6.2-GHz harmonic radiation. This design methodology is scalable; therefore, future iterations must precisely account for diode spacing to optimise the output of the targeted upconverted harmonics at different frequencies.

3.3 | Effects of Different LO Signals on the Metamaterial Structure

Although this study primarily focuses on optimising the 6.2-GHz harmonic, additional LO frequencies, specifically 2.1, 3 and 4.45 GHz were investigated to characterise their impact on the system's mixing performance. These frequencies were selected to evaluate the mixer's response across a broad spectral range. It was hypothesised that the diode arrangement, in conjunction

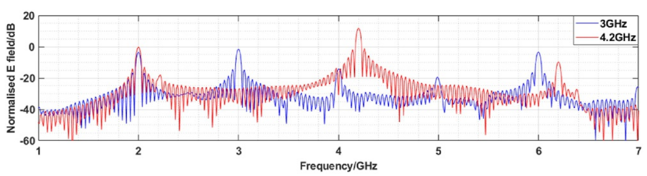

FIGURE 13 | Frequency spectra taken directly behind the structure when 3 and 4.2 GHz are used as stimuli for the LO layer.

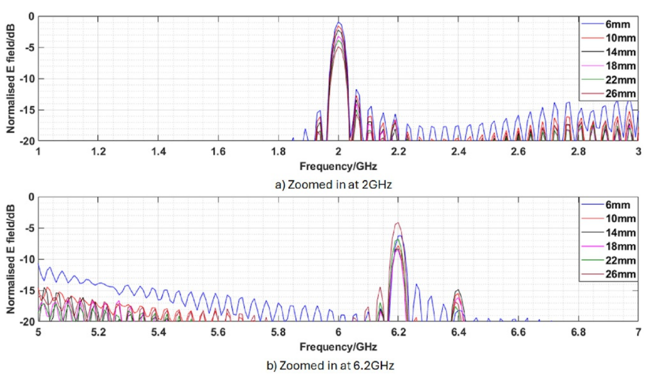

FIGURE 14 | Frequency spectra when 2 GHz illuminates the structure and 4.2 GHz is used as a stimulus for the LO layer when diode spacing is varied.

17518792, 2026, 1, Downloaded from https://ietresearch.onlinelibrary.wiley.com/doi/10.1049/rsn2.70150 by NICE, National Institute for Health and Care Excellence, Wiley Online Library on [11/05/2026]. See the Terms and Conditions (https://onlinelibrary.wiley.com/terms-and-conditions) on Wiley Online Library for rules of use; OA articles are governed by the applicable Creative Commons License

with the LO input frequency, could be used to control and maximise the magnitude of the upconverted harmonics. The 2-GHz incident frequency was kept constant throughout this evaluation.

Building on the optimisation study in Section 3.2, the 3D electric field distributions for various LO frequencies are detailed in Figure 15. Each LO signal was applied at 0 dBm to ensure a mixing effect while avoiding diode saturation. As shown in Figure 16, the magnitude of the electric fields coupling onto the mixer layer directly influences the induced surface currents. Analysis of Figure 16 shows that a 2.1-GHz LO signal induces the highest current amplitude $\left(4.82 \times 10^{-7}\ \mathrm{A/m}\right)$, whereas the 4.2-GHz LO signal results in the lowest $\left(4.33 \times 10^{-7}\ \mathrm{A/m}\right)$. The intermediate stimulus frequencies of 3 and 4.45 GHz induce currents of 4.37×10^{-7} A/m and 4.43×10^{-7} A/m, respectively. These results suggest that an optimal LO frequency when paired with the previously discussed diode separation can maximise signal conversion. Specifically, the high current induced by the 2.1-GHz LO signal is expected to produce a 4.1-GHz upconverted product with a greater amplitude than the 5-, 6.2- or 6.45-GHz harmonics generated by the other stimulus frequencies. This design methodology provides a framework for tailoring future metasurfaces to specific upconverted harmonic requirements.

The scattering spectra for LO frequencies of 2.1, 3, 4.2 and 4.45 GHz are presented in Figure 17 when the structure is illuminated with a 2-GHz signal. It was found that the amplitude of the LO signal increased with frequency with magnitudes of −7.3 dB, −1.4 dB, 11.9 dB and 12.9 dBV/m at 2.1, 3, 4.2 and 4.45 GHz, respectively. This is despite the signals all being input through the LO layer with equal amplitudes. This was a function of the transmission line's frequency-dependent S-parameters. Because the network was optimised for 4.2 GHz, the structure exhibits superior transmission efficiency at higher frequencies, resulting in the LO signal being radiated with its maximum amplitude at these frequencies.

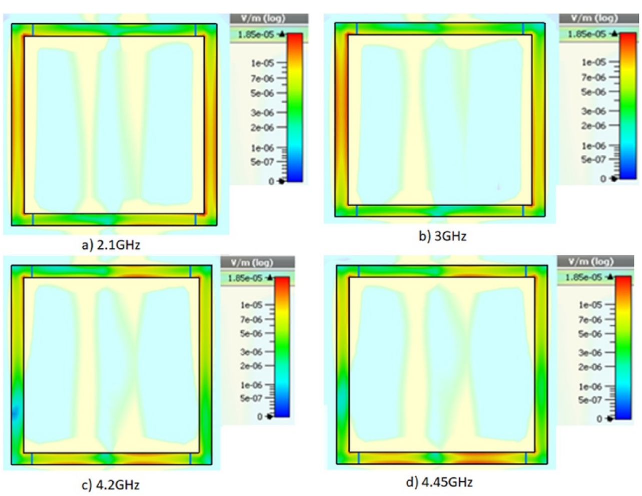

FIGURE 15 | Electric field distribution on mixer metamaterial of LO power when input power is 0 dBm for different frequencies.

Despite the variation in LO magnitudes, the resulting upconverted harmonics at 4.1, 5, 6.2 and 6.45 GHz have amplitudes of −15 dB, −19.3 dB, −9.6 dB and −8.3 dB, respectively. This reflects the results that were previously produced, whereby the higher LO amplitudes correspond to a greater mixing effect. Although a maximum reduction of − 3.4 dB was achieved at an LO frequency of 3 GHz, the signal remained at 0 dB when the LO frequency was 4.2 GHz. This is unexpected given that the 4.2-GHz LO produced a higher-magnitude upconverted harmonic. This discrepancy may be attributed to frequency-dependent scattering effects or structural resonances within the metamaterial, which alter the overall scattering parameters independently of the mixing efficiency.

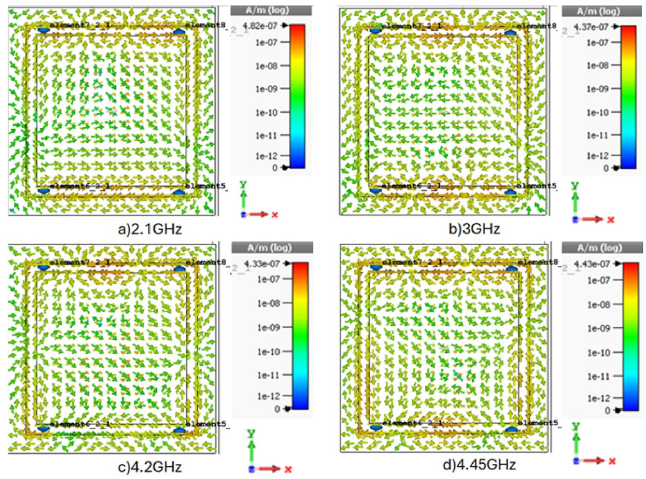

FIGURE 16 | Induced current distribution of different frequencies on metal around the aperture loop when LO power is 0 dBm.

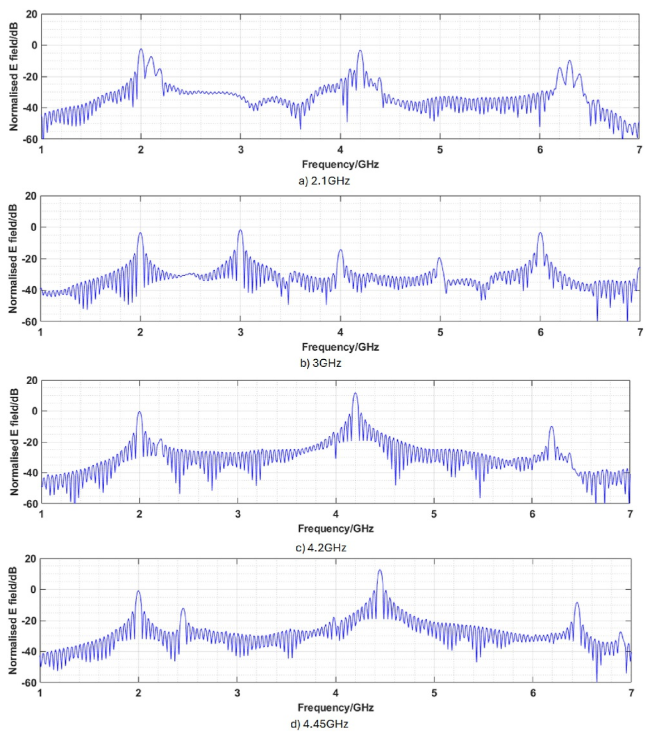

FIGURE 17 | Scattered frequency spectra taken when different stimuli are input through the LO layer with an input power of 0 dBm.

17518792, 2026, 1, Downloaded from https://ietresearch.onlinelibrary.wiley.com/doi/10.1049/rsn2.70150 by NICE, National Institute for Health and Care Excellence, Wiley Online Library on [11/05/2026]. See the Terms and Conditions (https://onlinelibrary.wiley.com/terms-and-conditions) on Wiley Online Library for rules of use; OA articles are governed by the applicable Creative Commons License

It is therefore assumed that, for different LO signals, a different input power could be required to achieve optimal mixer results due to the coupling and switching effects each LO stimulus contributes to the structure. When comparing to the previous results in Figure 18, we found that, when the power is increased, the structure appears to exhibit greater mixer effects. Because of the results seen in the polar plots in Figure 19 and when comparing to Figure 17, it can be assumed that the diodes, when the LO frequency is 4.2 GHz, have moved further into the nonlinear region and induced a greater mixing effect, creating a greater conversion effect. This can be attributed to a higher LO frequency which is input to the LO layer. This effect can thus be assumed for different frequencies whereby different power levels for each frequency will result in varying mixing effects, and by choosing the optimal power and LO frequency, the mixer structure exhibits fewer resistive effects on the reflectivity of the structure and greater conversion effects.

The electric field, current and scattering results all point to the effects of different LO frequencies on the mixer layer, and by using a suitable frequency, the upconverted harmonic can be optimised and maximised. This combination of factors and the input power through the LO layer are each used to switch on the diodes to a desired point in the nonlinear region, where mixing is maximised and the resistive effects on the reflectivity of the structure are minimised.

3.4 | Scattering Simulations and Nonlinear Performance

To simulate the structure, the mixer and LO layers from Section 2 were layered using the arrangement in Figure 1 and simulated with the mixer layer modelled as a 4 × 4 structure and the LO layer modelled as two separated lines running underneath it. The diodes on the mixer layer are modelled as point-to-point lumped element diodes using the corresponding separation detailed in Figure 2 and provide the desired mixer effects on the surface. Because the time-domain solver plane wave function is used only to measure the scattering from a surface, it displays the results of what is generated inside the bounding box, and an array of dipole antennas is used to illuminate the structure. The reflectivity and transmission results in Figure 20 were produced using a frequency-domain solver. Comparing the results in Figure 7, where the mixer layer alone was simulated, the overall reflectivity has increased from −31 dB to −24 dB, with a slight shift in frequency from 2.05 to

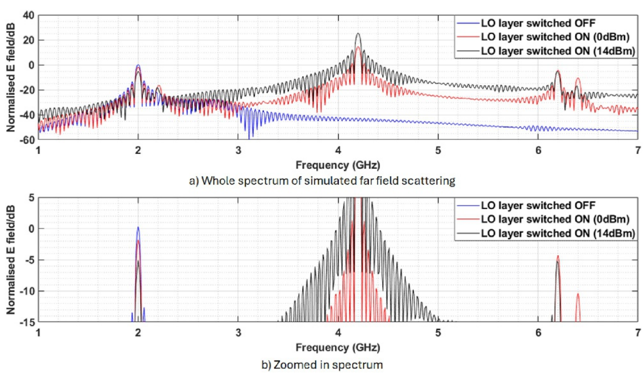

FIGURE 18 | Far-field scattering of harmonics at a 165° lobe.

1.98 GHz. This is due to the added effect of the LO layer that contributes to this slight shifting; however, the structure may still be used at 2 GHz.

Following on from the reflectivity and transmission results, simulations were carried out using the time-domain solver to evaluate the scattering when f_i and f_{LO} signals were generated as sinusoidal waves using MATLAB and input through the illuminating source and LO layer. In this simulation, an array of dipoles was used to illuminate the structure so that the scattering of the illuminating 2-GHz signal could be evaluated. Simulations were performed when the LO layer was switched off and switched on with a 14-dBm signal to ensure mixing across the structure. A 4.2-GHz signal is input through waveguide ports at the edge of the LO layer down through the inputs of the transmission lines to provide stimulus and f_{LO} to the mixer structure that then upconverts the illuminating 2-GHz signal. This produced the results in Figure 21 where the measurements were taken directly underneath the structure. When examining the results in Figure 21a, where the top and bottom

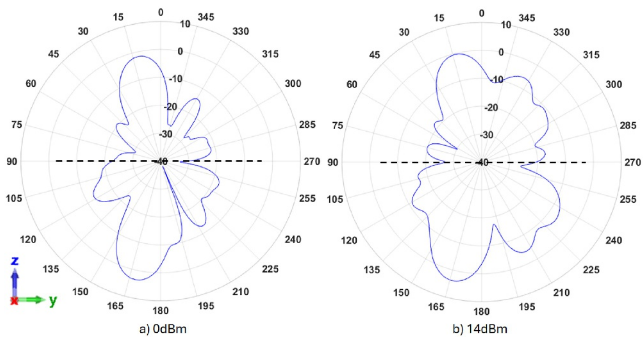

FIGURE 19 | Electric field (dBV/m) results for different input powers.

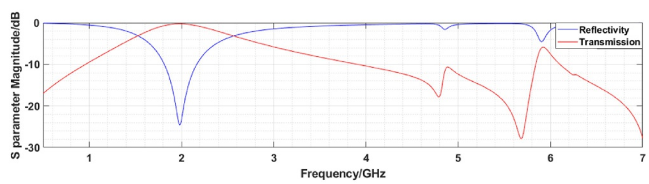

FIGURE 20 | Reflectivity and transmission of whole structure.

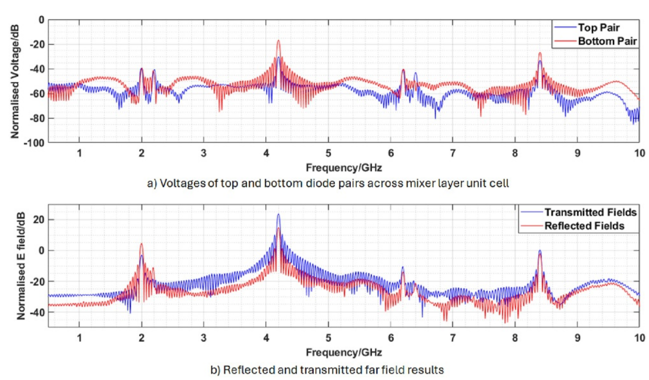

FIGURE 21 | Lumped element and scattering results with an input power of 14 dBm.

17518792, 2026, 1, Downloaded from https://ietresearch.onlinelibrary.wiley.com/doi/10.1049/rsn2.70150 by NICE, National Institute for Health and Care Excellence, Wiley Online Library on [11/05/2026]. See the Terms and Conditions (https://onlinelibrary.wiley.com/terms-and-conditions) on Wiley Online Library for rules of use; OA articles are governed by the applicable Creative Commons License

diode pairs are shown, it was found that the desired 6.2-GHz harmonic was generated alongside a second 8.4-GHz signal. This was expected, as the 8.4-GHz signal was generated by the doubling of the 4.2-GHz f_{LO} signal, which appears in the diode results as the largest generated harmonic with amplitudes of −33.1 dB and −26.6 dB for the top and bottom diode pairs, respectively. This was expected because the amplitude of the 4.2-GHz signal is larger than the 2-GHz signal, which, due to mixer theory and as found in common mixer circuits [29–31], will have an impact on the overall amplitude of the 6.2-GHz signal. When examining the 2.2- and 6.2-GHz harmonics in Figure 19a, these were the second-largest harmonics and are of similar amplitudes between −41 dB and −40 dB. These are the upconverted and downconverted products of the mixing of the f_i and f_{LO} signals and will be radiated by the structure. Other harmonics exist, such as the 6.4-GHz harmonic, which is the product of the 8.4-GHz harmonic mixing with the 2-GHz input signal and, as such, is lower than the $f_i \pm f_{LO}$ products with an amplitude of −43 dB.

The 6.2- and 8.4-GHz harmonics were then observed in the scattering plot in Figure 21b, where in the transmitted fields, these harmonics have amplitudes of −10.4 and 0 dB, respectively. A similar effect was found in the reflected fields, whereby the 6.2- and 8.4-GHz harmonics are −13.9 dB and −2.8 dB, respectively. These results were smaller than expected given the change in the 2-GHz signal, and as such, a greater study of the scattering of the 6.2-GHz signal was required. The 2-GHz signal is found to be attenuated when comparing the transmitted and reflected fields, as there is a difference of 8 dB; however, it is found that the 6.2-GHz signal is not as high as this harmonic, and thus further probes are required to be placed around the structure to determine the direction and magnitude of the scattering to determine where maxima are occurring. The 8.4-GHz harmonic is also observed to be larger than the 6.2-GHz signal, which is expected due to the voltage results across the diodes; however, from looking at these results, a larger 6.2-GHz harmonic was expected, leading to an additional investigation of this signal.

To study the scattering of the 6.2-GHz harmonic around the mixer structure, E-field polar plots were generated for the $\phi = 270°$ cut, as shown in Figure 19. These plots detail the scattering at LO input powers of 0 dBm and 14 dBm, with a black dotted line superimposed to denote the mixer structure. From the two plots, we see at 165° a main lobe at amplitudes of 4 dBV/m and 3 dBV/m; when the power was increased, a second lobe began to appear at 235° that tends towards −5 dBV/m at 14 dBm. Other lobes are also observed at 15° and 205°; however, in the scope of this research, the lobes at 165° and 235° were examined further.

To examine the far-field scattering at the 165° lobe, the spectra in Figure 18 were analysed to find the maximum 6.2-GHz harmonic. Figure 18a illustrates the 1–7-GHz spectrum, where the 4.2-GHz LO signal has amplitudes of 14.6 and 25.4 dB at LO input powers of 0 dBm and 14 dBm, respectively. These levels confirm that the LO signal successfully biases the diodes compared to the "off" state. Consistent with the polar plots in Figure 19, the generated 6.2-GHz harmonic at the 165° lobe is significantly larger than those in Figure 21b, with its amplitude approaching that of the 2-GHz signal. These 1D scattering results, measured with far-field probes, verify the previously observed scattered lobes. In Figure 18b, a zoomed-in spectrum is presented. In these results, we see that the 2-GHz signal was attenuated by approximately 6 dBV/m (reducing from 0 dBV/m to −5.5 dBV/m) when comparing the off and 14-dBm states, and this is attributed to the mixing effect. As the LO power increases, diode saturation leads to more mixing and conversion. This saturation effect is further seen in Figure 18b, where the 6.2-GHz harmonic appears to decrease as the LO power is switched from 0 dBm to 14 dBm. This follows the trend observed in the polar plots at 165°, where the harmonic magnitude diminishes as LO power increases. Furthermore, as the LO power rises, new lobes emerge at other coordinates such as 235°, suggesting that diode saturation can shift the scattering direction of the generated 6.2-GHz harmonic.

Other signals were generated, such as the downconverted component at 2.2 GHz corresponding to the $f_{LO} - f_i$ mixing product. This component exhibits an amplitude of −16 dB, which decreases as the LO input power increases; however, similar to the 6.2-GHz case, these harmonics are expected to increase at different spatial points around the structure. A final scattering product appears at 6.4 GHz, corresponding to the $2f_{LO} - f_i$ harmonic. As predicted by the diode voltages in Figure 21a, this signal remains low, measuring −11.1 dB at an LO power of 0 dBm and dropping to −16.9 dB at 14 dBm. This suggests a pattern similar to the 6.2-GHz polar plots, where the amplitude decreases at one angle while increasing at another. The results across these frequencies indicate that a consistent physical effect occurs regardless of the LO frequency, a trend, that is, expected to persist for other generated harmonics.

3.5 | Adding the Absorbing Layer to the Structure

With the nature of the far-field scattering of upconverted harmonics studied, the next step involved integrating the absorbing layer conceptualised in Section 2.4 to absorb the 6.2-GHz harmonics generated by the mixer layer. To design an optimal absorber that operates at 6.2 GHz, parameter sweeps of the distance between the resistive FSS and ground plane D were carried out. Following this, the resistance of components on the absorber layer was varied to optimise the structure's reflectivity. The results of these sweeps are presented in Figure 22.

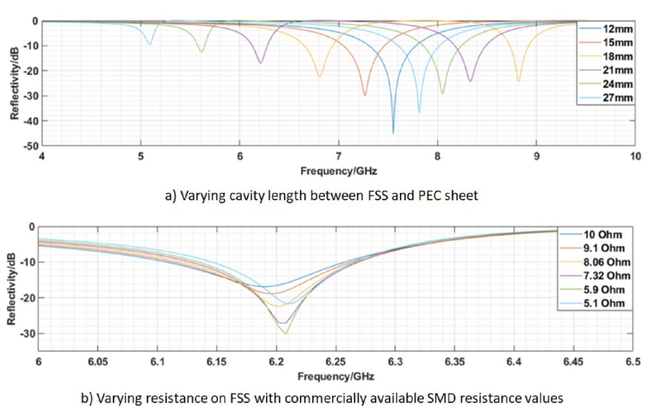

FIGURE 22 | Results of initial simulation of absorber.

17518792, 2026, 1, Downloaded from https://ietresearch.onlinelibrary.wiley.com/doi/10.1049/rsn2.70150 by NICE, National Institute for Health and Care Excellence, Wiley Online Library on [11/05/2026]. See the Terms and Conditions (https://onlinelibrary.wiley.com/terms-and-conditions) on Wiley Online Library for rules of use; OA articles are governed by the applicable Creative Commons License

By sweeping the distance between the FSS and ground plane for an initial resistance of 10Ω, the ideal value of D was found. This process is shown in Figure 22a, where the distance is swept in 3 mm increments to coincide with the size of spacers that are used in the fabricated structures. We find here that the optimal distance was 21 mm. This is larger than the $\frac{\lambda}{4}$ spacer requirement found in classic absorber designs; the surface has an equivalent parallel LC circuit topology with the inductance of the surface dominating at low frequencies, and as such, the spacer needs to have an equivalent capacitive impedance to achieve resonance, leading to an electrically thicker structure.

Following the initial distance sweep, the reflectivity of the structure was optimised by selecting a resistor value that provided appropriate matching to the free-space impedance, η_o. Figure 22b illustrates the results of this optimisation, where the resistance was swept across commercially available SMD resistor values. It was determined that 5.9 Ω resistors achieved a reflectivity magnitude of −28 dB at 6.2 GHz. It should be noted that this resistance is a practical selection based on commercial availability rather than a theoretical optimum. This configuration provides an absorber tuned to this frequency, intended to suppress the 6.2-GHz signals radiated by the structure when the 2-GHz f_i signal mixes with the 4.2-GHz f_{LO} signal.

The next stage involved assessing the absorber's performance within the full structure. Simulations were conducted with the absorber positioned behind the mixer/LO layers. A parameter sweep was performed on the separation between the mixer layer and the ground plane, with the diodes modelled as 1MΩ resistors to represent an off state. By varying the distance from 36 to 57 mm in 3 mm increments, it was determined that a 54-mm separation was required to provide resonance at 2 GHz. These results are presented in Figure 23a, where the simulated reflectivity is −1.4 dB at 2.03 GHz. To evaluate how diode resistance influences the absorption, Figure 23b illustrates the effect of varying the resistance from 1 MΩ to 300 Ω. This transition simulates the diodes switching from an open-circuit to an ‘on’ state. At a resistance of 300 Ω, the structure achieves a minimum reflectivity magnitude of −25 dB at 2 GHz. This investigation shows that both absorption, from the diode resistance, and frequency conversion, from mixing, could contribute to the final reflectivity of the structure.

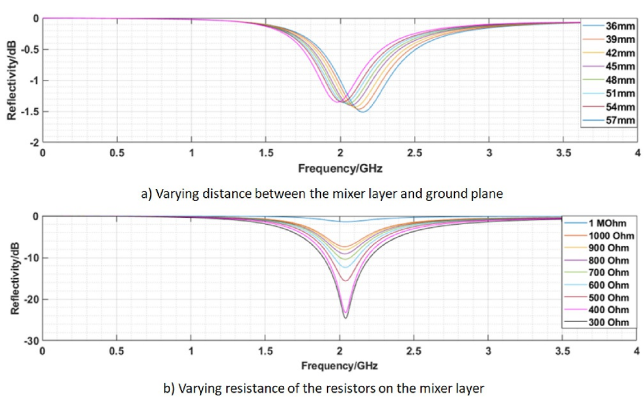

FIGURE 23 | Reflectivity results of whole structure.

4 | Fabrication/Measurement

4.1 | Measurements—Reflectivity and Transmission

To verify the simulated reflectivity and transmission results in Figure 20, measurements were carried out using an NRL arch and transmission systems (Figure 24a,b) and a fabricated 8 × 8 mixer structure was tested. The final dimensions of the mixer layer are 318.4 mm × 318.4 mm, fabricated on 1 mm-thick FR-4, whereas the LO layer is 469.4 mm × 318.4 mm, fabricated on a 1.2-mm-thick FR-4. A design trade-off was made between electrical size (approximately 2λ) and edge diffraction; although a larger sample would have been preferable to minimise edge effects, these dimensions were selected as a practical compromise. The two measurement environments differ significantly in character. The NRL arch (Figure 24a) is located within an anechoic chamber to minimise multipath reflections. In contrast, the transmission set-up (Figure 24b) is subject to the inherent scattering of a standard laboratory setting. Consequently, frequency spectra derived from the transmission measurements are expected to exhibit higher noise levels and interference from reflections off the surrounding laboratory environment.

The results (Figure 25a,b) (reflectivity) (transmission) indicate that the integration of the BAT15 diodes causes the operational frequency of the FSS to shift from 1.98 to 1.75 GHz. This shift is attributed to the parasitic reactance and resistive effects of the diodes. A comparison between the simulated and measured “off” state reflectivity reveals a magnitude shift of 6.7 dB, moving from a simulated −24.5 dB to a measured −17.8 dB. This discrepancy is likely due to diode parasitic capacitance and resistance, with minor structural warping causing the measured reflectivity and transmission to occasionally rise slightly above 0 dB, though this effect remained minimal (under 2 dB). The structure's response varies significantly with LO frequency. At an f_{LO} of 2.1 GHz, a substantial amplitude shift is observed, with reflectivity reaching −11.3 dB at 1.75 GHz. This suggests that the diodes are more heavily biased at this frequency, leading to increased resistive effects. Conversely, a 3-GHz LO stimulus produces a minimal shift (measured at −17.4 dB), whereas 4.2 and 4.45 GHz stimuli result in intermediate shifts of −14.25 dB and −13.75 dB, respectively. These trends suggest that the

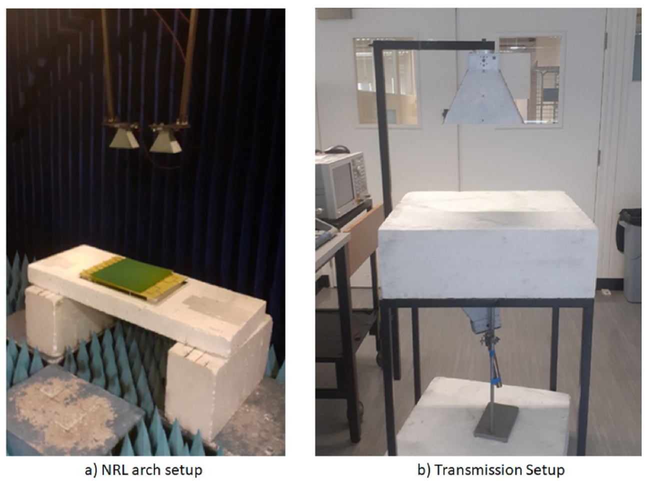

FIGURE 24 | Experimental set-ups.

17518792, 2026, 1, Downloaded from https://ietresearch.onlinelibrary.wiley.com/doi/10.1049/rsn2.70150 by NICE, National Institute for Health and Care Excellence, Wiley Online Library on [11/05/2026]. See the Terms and Conditions (https://onlinelibrary.wiley.com/terms-and-conditions) on Wiley Online Library for rules of use; OA articles are governed by the applicable Creative Commons License

2.1-GHz stimulus drives the diodes further into saturation. Similar trends are observed in the transmission results. The operating frequency shifted to 1.75 GHz, with amplitudes of −0.26 dB (simulated) and 0.96 dB (measured) when the LO layer is in the 'off' state. The measured transmission exceeding 0 dB is attributed to environmental noise and reflections inherent to the experimental set-up. As with reflectivity, the 2.1-GHz LO signal induced the greatest amplitude shift, decreasing to −4 dB at 1.75 GHz, whereas the 3-GHz signal showed a negligible 1-dB difference between states. These results imply that different levels of mixing and nonlinear behaviour can be expected depending on the saturation level induced by the specific LO frequency.

The measured S-parameters for the LO layer are presented in Figure 26a,b. The measured S_{11} at 4.45 GHz deviates from the simulated −22.2 dB to −27.6 dB. Although some deviation is expected due to the power splitter used to feed the LO layer, the larger variance is likely attributable to manufacturing tolerances, SMA connector effects and cables. Despite these deviations, the S_{11} magnitude at the 4.45-GHz target frequency remains below −20 dB, indicating minimal reflections. The measured S_{21} results (Figure 26b) follow the simulated profile but exhibit higher overall losses, which increase with frequency. This is a known characteristic of the FR-4 substrate, which becomes more lossy at higher frequencies. However, the deviation at 4.45 GHz is acceptable, shifting from a simulated −10.23 dB to a measured −12 dB. In summary, although the LO layer is more lossy than predicted, the additional losses are not sufficient to render the layer redundant. The performance at the desired 4.45-GHz frequency remains close to the design targets, ensuring that the LO layer will function effectively within the integrated system.

4.2 | Measurements—Far-Field Scattering

To verify the simulated far-field scattering, the experimental set-up shown in Figure 24b is employed. The sample was positioned on the test bed and illuminated with a 1.75-GHz signal at an input power of 10 dBm. This frequency was selected to align with the resonant frequency identified in prior measurements. Scattering was measured in dBm using a spectrum analyser and a receiving horn antenna positioned beneath the sample. Figure 27 presents these results across five different configurations. Figure 27a,b illustrates the response at various LO signal frequencies with 20 dBm input power, Panel (c) shows the system with the LO layer deactivated, Panel (d) displays a metallic reference plate of equivalent dimensions, and Panel (e) represents the open test bed. The results from Figure 27d,e serve as benchmarks for the maximum and minimum expected scattering, thereby defining the dynamic range of the measurement. As shown in Figure 27a, the reduction of the 1.75-GHz signal depends significantly on the LO layer input frequency. These results mirror the trends in Figure 25; as shown in Figure 27b, we find that a 2.1-GHz LO input yields a 1.75-GHz amplitude of −8.21 dBm, whereas an LO input of 3 GHz results in a 1.75-GHz amplitude of −4.03 dBm. When the LO layer is deactivated (Figure 27c), the amplitude is −3.1 dBm. These observations correlate with the transmission and reflectivity data, where the greatest impact on the transmission parameter occurs at an LO frequency of 2.1 GHz. Similarly, LO frequencies of 4.2 and 4.45 GHz produced 1.75 GHz amplitudes of −6.76 dBm and −6.47 dBm, respectively, further confirming the previously observed trends. A comparison with the reference cases (Figure 27d,e) representing the open test bed with a 1.75-GHz amplitude of −2.87 dBm and the metallic sheet only, where the 1.75-GHz amplitude is −16.69 dBm, indicates that the 1.75-GHz signal magnitude for any given stimulus remains within this dynamic range. The variations in amplitude are attributed to the combination of reflectivity and frequency conversion provided by the mixer structure. This is further evidenced in Figure 27b, where the 2.1-GHz LO signal provides a more pronounced reduction in the 1.75-GHz signal compared to the 3-GHz LO signal. Finally, Figure 27a illustrates the magnitudes of the converted harmonics. For the various LO inputs, the sum-frequency harmonics $(f_i + f_{LO})$ at 3.85, 4.75, 5.95 and 6.2 GHz yielded amplitudes of −38.19, −42.4, −37.05 and −37.9 dBm, respectively. Because of the angular nature of harmonic scattering, the results at 5.95 and 6.2 GHz represent local maxima for the current horn position. It is therefore anticipated that higher amplitudes for the 3.85- and 4.75-GHz harmonics could be measured if the receiving horn were repositioned to locate their respective main lobes. The magnitude of the 6.2-GHz harmonic aligns with the radiation patterns shown in Figure 19, suggesting that a similar spatial distribution exists for the other generated harmonics.

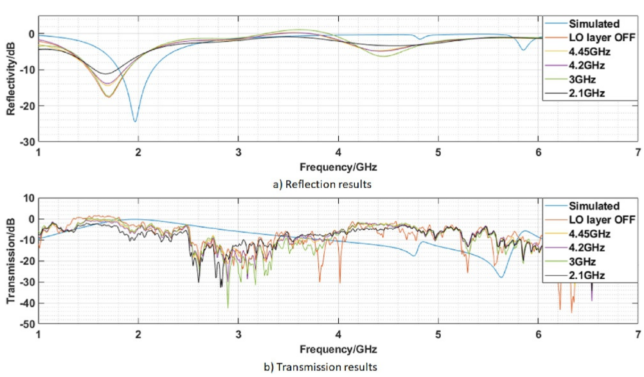

FIGURE 25 | Reflectivity and transmission results when the LO power is 20 dBm at different frequencies.

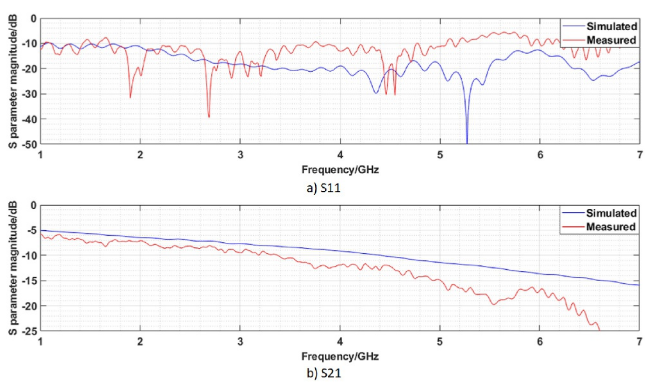

FIGURE 26 | Measured and simulated results for S_{11} and S_{21} of the LO layer.

17518792, 2026, 1, Downloaded from https://ietresearch.onlinelibrary.wiley.com/doi/10.1049/rsn2.70150 by NICE, National Institute for Health and Care Excellence, Wiley Online Library on [11/05/2026]. See the Terms and Conditions (https://onlinelibrary.wiley.com/terms-and-conditions) on Wiley Online Library for rules of use; OA articles are governed by the applicable Creative Commons License

4.3 | Measurements—Fabricated Absorber

Following the scattering results that verify mixing, the simulated absorber performance must be validated. The 6.2-GHz absorber, conceptualised in Section 3.5, was fabricated as a 318.4 × 477.6 mm structure (Figure 28a), slightly larger than the LO layer and utilising an aluminium ground plane. The absorber was positioned behind the mixer structure, as shown in the side profile in Figure 28b. Elastic bands were employed to minimise structural warping, whereas 3 mm polystyrene spacers maintained the necessary cavity between constituent layers.

Using the set-up from Figure 24a, the measured reflectivity of the fabricated absorber was compared to simulations using 5.9 Ω resistors. As shown in Figure 29, an absorption null of −26.8 dB was measured at 6.2 GHz, correlating well with the simulated value of −30.3 dB. A second null appears at 8.37 GHz with an amplitude of −17.2 dB. Additionally, some results between 6.5 and 7.5 GHz slightly exceed 0 dB. This result is likely due to structural bowing causing parabolic reflection effects compared to the flat metallic calibration plate. Furthermore, edge effects and the wide beamwidth of the horn antennas in this frequency range likely introduced unwanted reflections. Although a larger sample (≈10λ or 1500 mm) would mitigate these distortions, the current set-up remains sufficient for this proof-of-concept.

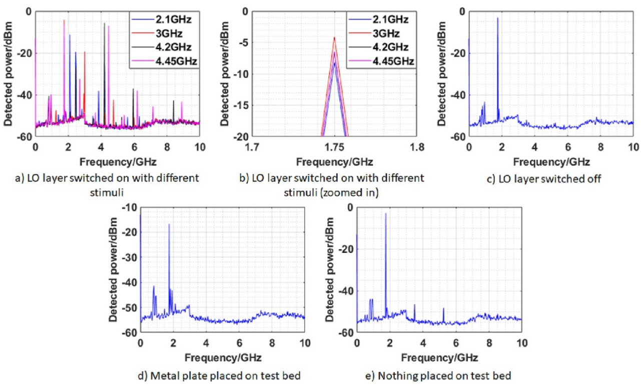

FIGURE 27 | Scattering measurements when different stimuli are input through the LO layer.

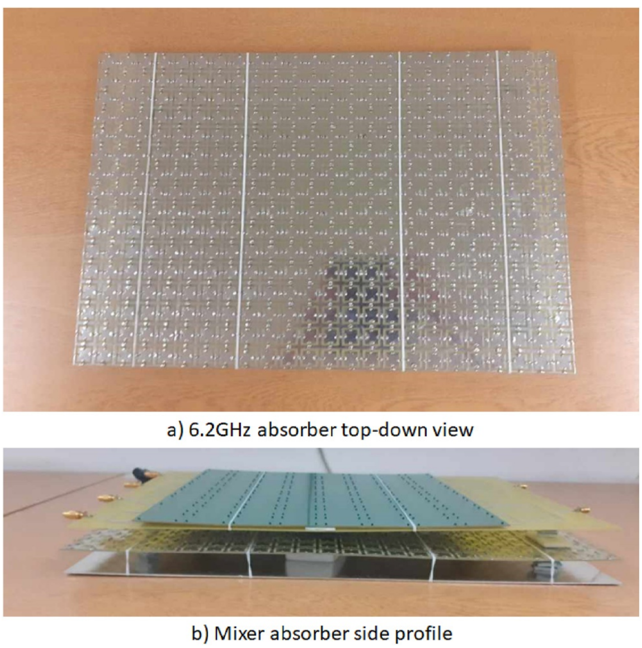

FIGURE 28 | Fabricated absorber, top-down view and side profile of mixer-absorber structure.

To verify the integrated results from Figure 23, the separation between the mixer and absorber was adjusted using 3 mm spacers. Experimental results (Figure 30a) indicate an optimal cavity depth of 42 mm, a departure from the 54-mm predicted by simulation. This discrepancy is attributed to the parasitic capacitance of the diodes, which makes the structure appear electrically thicker than the idealised model. Figure 30b illustrates the effect of varying the 4.2-GHz LO power. When the LO layer is inactive, reflectivity is −5 dB. As input power increases towards 20 dBm, the diodes reach their switching threshold, acting as resistive elements and transitioning the structure into an absorbing state, as predicted in Figure 23b.

These results follow the scattering results in Figures 25 and 27, where, when the same methodology was employed, the diodes on the mixer layer begin to switch on, activating the nonlinear mixer and resistive effects that characterise the mixer metamaterial.

The frequency sensitivity of the LO layer is examined in Figure 31 using 2.1, 3, 4.2 and 4.45 GHz signals at 20 dBm. The trends align

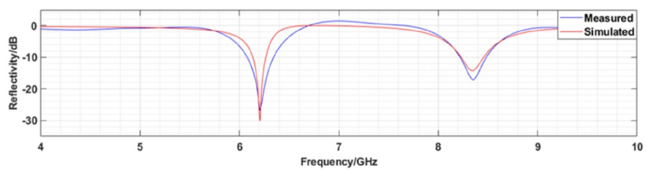

FIGURE 29 | Simulated and measured reflectivity results of a 6.2-GHz absorber.

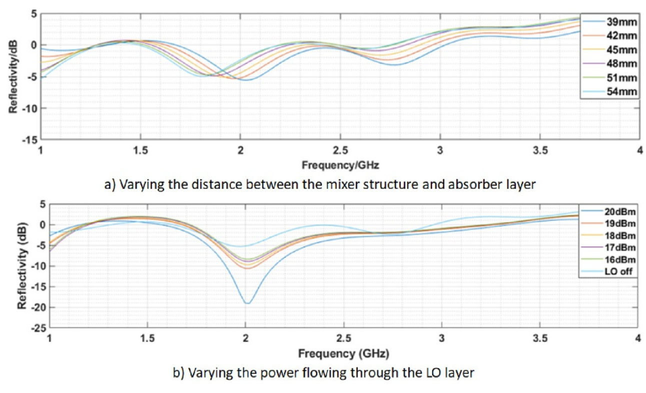

FIGURE 30 | Simulated and measured reflectivity results of a 6.2-GHz mixer-absorber structure.

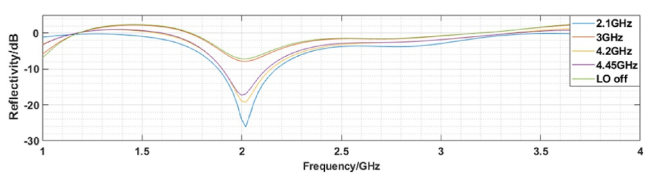

FIGURE 31 | Simulated and measured reflectivity results of a 6.2-GHz absorber.

17518792, 2026, 1, Downloaded from https://ietresearch.onlinelibrary.wiley.com/doi/10.1049/rsn2.70150 by NICE, National Institute for Health and Care Excellence, Wiley Online Library on [11/05/2026]. See the Terms and Conditions (https://onlinelibrary.wiley.com/terms-and-conditions) on Wiley Online Library for rules of use; OA articles are governed by the applicable Creative Commons License

TABLE 5 | Comparison of current work with existing literature.

Reference	Scattering reduction (dB)	f_0 (GHz)	d/λ_0	Reduction method
This paper	19.8	2.00	0.132	Mixer diodes and absorber
[8]	34.5	17.0	0.588	Concentric-SRR arc-dipole
[15]	9.3	10.2	1.022	Mixer components
[25]	20.0	110 and 290	4.03 and 10.6	Absorber

with Figure 25, where, at an LO frequency of 3 GHz, the reflectivity of −8 dB is nearly identical to the "off" state at −7.75 dB, indicating minimal activation. Conversely, when the LO frequency is 4.2 and 4.45 GHz, the reflectivity increases to −17.8 dB and −19.2 dB, respectively, as the diodes begin to switch on. The most significant effect occurs at 2.1 GHz, where a reflectivity of −26 dB was measured. This confirms that the LO frequency profoundly influences diode activation. This increased response at 2.1 GHz is likely due to enhanced coupling between the LO transmission lines and the mixer layer, inducing larger surface currents. This experimental finding is consistent with the simulated surface currents in Figure 16, confirming that the 2.1-GHz signal provides the most efficient frequency conversion.

5 | Conclusions and Future Work

An in-depth analysis of a mixer metamaterial, coupled to an LO layer, has been provided and gives an understanding of how the LO layer can be used to provide frequency conversion when a low-frequency plane wave illuminates the structure. By analysing surface currents, field distributions and scattering parameters, it was demonstrated that LO frequency tuning significantly modifies harmonic generation. Specifically, simulations and measurements both indicate that a 2.1-GHz LO frequency induces a stronger resistive effect than a 3-GHz input. The minimal difference in harmonic magnitude between these frequencies suggests that the perceived conversion loss is partially governed by the resistive states of the embedded diodes, which cause the structure to reflect the incident 2-GHz signal rather than purely converting it.

This work was further expanded by integrating a metamaterial absorber behind the mixer structure to suppress the 6.2-GHz sum-frequency harmonic. The absorption depth was found to be highly sensitive to the LO input frequency at 2.1 GHz; the null depth increases significantly compared to 3 GHz due to the enhanced resistive switching of the mixer diodes. This verifies the presence of simultaneous resistive and mixing effects and suggests that harmonic generation can be further optimised.

Table 5 compares this work against existing literature. Although the authors in Ref. [8] achieve a higher reduction of 34.5 dB, it operates over a narrow bandwidth. In contrast to the down-conversion focus of Ref. [15] (which utilised a directly connected 2.2-dBm LO signal), this research achieves a 19.8-dB reduction without DC biasing or direct LO injection, albeit at the cost of higher required LO power. Furthermore, although the absorber in Ref. [25] achieved a 20-dB reduction using a complex multilayered structure with a high d/λ_0 ratio, this study achieves comparable results using a simpler, low-profile absorber. Future work will focus on maximising the $f_i + f_{LO}$ harmonic, which was lower than theoretically anticipated. Potential improvements include the implementation of high-Q diodes and the optimisation of the LO layer to minimise coupling losses. Additionally, investigating the power ratios between the incident f_i and LO signals will help identify the saturation points for harmonic generation. Finally, exploring Jaumann absorbers or ohmic-sheet Salisbury designs could provide a thinner, broadband solution for suppressing other mixing products, such as $f_i - f_{LO}$ or $2f_i$ harmonics.

Author Contributions

Douglas A. Bowe: conceptualization, formal analysis, investigation, methodology, writing – original draft. **Kenneth L. Ford:** conceptualization, funding acquisition, project administration, supervision, writing – review and editing. **Alan Tennant:** supervision.

Acknowledgements

This work was sponsored and funded by the UK's Dstl (Defence Science and Technology Laboratories).

Conflicts of Interest

The authors declare no conflicts of interest.

Data Availability Statement

The data that support the findings of this study are available from the corresponding author upon reasonable request.

References

1. B. Chambers, *Tunable Radar Absorbers Using Frequency Selective Surfaces* Vol. 11 (Institution of Engineering and Technology (IET), 2001), 593–597.

2. J. Du, J. Fang, X. Wang, et al., "Equivalent Analysis Method for Coupling Scattering of Low Scattering Ships in Sea Environment," in *Proceedings of 2024 International Conference on Energy and Electrical Engineering, EEE 2024* (Institute of Electrical and Electronics Engineers Inc., 2024).

3. R. Zhao, L. Shao, and W. Zhu, "Switchable Metamaterial Absorber and Reflector Using Pin Diodes," in *2019 International Conference on Microwave and Millimeter Wave Technology, ICMMT 2019 - Proceedings*, Vol. 5 (Institute of Electrical and Electronics Engineers Inc., 2019).

4. I. Gerafentis and A. Feresidis, "Design of Tunable Millimetre-Wave Pass-Band Fss Unit-Cell Loaded With Gaas air-Bridged Schottky Diodes," in *2022 16th European Conference on Antennas and Propagation* (EuCAP, 2022).

5. J. Zhao, Q. Cheng, J. Chen, M. Q. Qi, W. X. Jiang, and T. J. Cui, "A Tunable Metamaterial Absorber Using Varactor Diodes," *New Journal of*

17518792, 2026, 1, Downloaded from https://ietresearch.onlinelibrary.wiley.com/doi/10.1049/rsn2.70150 by NICE, National Institute for Health and Care Excellence, Wiley Online Library on [11/05/2026]. See the Terms and Conditions (https://onlinelibrary.wiley.com/terms-and-conditions) on Wiley Online Library for rules of use; OA articles are governed by the applicable Creative Commons License

Physics 15 (2013): 043049, https://doi.org/10.1088/1367-2630/15/4/043049.

6. A. Tennant and B. Chambers, “A single-layer Tuneable Microwave Absorber Using an Active Fss,” *IEEE Microwave and Wireless Components Letters* 14, no. 1 (2004): 46–47, https://doi.org/10.1109/lmwc.2003.820639.

7. J. B. Hacker, R. M. Weikle, M. Kim, M. P. D. Lisio, and D. B. Rutledge, “A 100-Element Planar Schottky Diode Grid Mixer,” *IEEE Transactions on Microwave Theory and Techniques* 40, no. 3 (1992): 557–562, https://doi.org/10.1109/22.121732.

8. P. A. Kumari, M. V. Narayana, G. Immadi, Y. Solunke, and K. V. P. Kumar, “Design and Performance Evaluation of a Narrow-Band Metasurface Radomes for Reduction of Rcs in Stealth Applications,” *Progress in Electromagnetics Research C* 164 (2026): 186–194, https://doi.org/10.2528/pierc25111403.

9. D. Ferreira, R. F. Caldeirinha, I. Cuinas, and T. R. Fernandes, “Square Loop and Slot Frequency Selective Surfaces Study for Equivalent Circuit Model Optimization,” *IEEE Transactions on Antennas and Propagation* 63 (9 2015): 3947–3955, https://doi.org/10.1109/tap.2015.2444420.

10. Y. Xu and M. He, “Design of Multilayer Frequency-Selective Surfaces by Equivalent Circuit Method and Basic Building Blocks,” *International Journal of Antennas and Propagation* 2019 (2019): 1–13, https://doi.org/10.1155/2019/9582564.

11. B. Chambers and K. L. Ford, “Topology for Tunable Radar Absorbers,” *Electronics Letters* 36, no. 15 (2000): 1304–1306, https://doi.org/10.1049/el:20000941.

12. K. Chang, S. I. Kwak, and Y. J. Yoon, “Equivalent Circuit Modeling of Active Frequency Selective Surfaces,” in *2008 IEEE Radio and Wireless Symposium, RWS* (2008), 663–666.

13. X. Lei, X. Long, L. Luo, X. Li, X. Liu, and M. Zhou, “A Broadband Tunable Absorber Based on a Pin Diode-Loaded Frequency Selective Surface,” in *Proceedings - 2022 International Conference on Computing, Communication, Perception and Quantum Technology, CCPQT 2022* (2022), 324–327.

14. M. Elsaadi, H. Elsaady, R. Matroud, and O. Juakah, “High Driven Sub-Harmonically up-Conversion Mixers Based Schottky Diodes,” in *2022 IEEE 2nd International Maghreb Meeting of the Conference on Sciences and Techniques of Automatic Control and Computer Engineering, MI-STA 2022 - Proceeding* (Institute of Electrical and Electronics Engineers Inc., 2022), 340–344.

15. J. B. Hacker, R. M. Weikle, M. Kim, and D. B. Rutledge, “A 100-Element Schottky Diode Grid Mixer,” in *AP-S International Symposium (Digest) (IEEE Antennas and Propagation Society)*, Vol. 1 (Publ by IEEE, 1991), 146–149, https://doi.org/10.1109/aps.1991.174794.

16. R. R. Swisher, F. Lecuyer, I. F. F. Chio, J. C. Chiao, and M. P. D. Lisio, “Balanced Diode Grid Mixer,” *IEEE MTT-S International Microwave Symposium Digest* 2 (1999): 555–558, https://doi.org/10.1109/MWSYM.1999.779823.

17. M. Oliveira, C. D. M. Cheung, A. Al-Zayed, et al., “A High-Linearity 100-Element Diode Grid Mixer,” *IEEE Transactions on Antennas and Propagation* 50, no. 5 (2002): 698–702, https://doi.org/10.1109/tap.2002.1011237.

18. R. S. Anwar, L. Mao, and H. Ning, “Frequency Selective Surfaces,” *A review* 9 (2018), https://doi.org/10.3390/app8091689.

19. W. Li, C. Wang, Y. Zhang, and Y. Li, “A Miniaturized Frequency Selective Surface Based on Square Loop Aperture Element,” *International Journal of Antennas and Propagation* 2014 (2014): 1–6, https://doi.org/10.1155/2014/701279.

20. H. M. Aumann and N. W. Emanetoglu, “A Wideband Harmonic Radar for Tracking Small Wood Frogs,” in *IEEE National Radar Conference - Proceedings* (Institute of Electrical and Electronics Engineers Inc., 2014), 108–111.

21. N. Nourshamsi, S. Vakalis, and J. A. Nanzer, “Joint Detection of Human and Object Motion Using Harmonic Micro-Doppler Radar and Harmonic Tags,” *IEEE Antennas and Wireless Propagation Letters* 19 (6 2020): 930–934, https://doi.org/10.1109/lawp.2020.2983012.

22. D. A. Bowe, K. L. Ford, and A. Tennant, “An Upconverting Superheterodyne Metamaterial,” in *17th European Conference on Antennas and Propagation, Eucap 2023* (Institute of Electrical and Electronics Engineers Inc., 2023).

23. G. Gao, J. Dai, S. Liu, and Q. Cheng, “Low in-Band-rcs Tightly Coupled Dipole Array Based on Metamaterial Absorber,” in *2024 International Applied Computational Electromagnetics Society Symposium, ACES-China 2024 - Proceedings* (Institute of Electrical and Electronics Engineers Inc., 2024).

24. Y. K. Jung and B. Lee, “Beam Scannable 4 × 4 Patch Array Antenna Using Tunable Metamaterial Phase Shifters,” in *2014 8th International Congress on Advanced Electromagnetic Materials in Microwaves and Optics, METAMATERIALS*, Vol. 11 (Institute of Electrical and Electronics Engineers Inc., 2014), 355–357.

25. A. P. Sohrab and Z. Atlasbaf, “A Thin Wideband Absorber With Uniform Response in x-Band,” in *2012 15th International Symposium on Antenna Technology and Applied Electromagnetics, ANTEM 2012*, 2012).

26. Z. Zhang, S. Yang, Y. Ma, Y. Chen, and S. Qu, “Scattering Control of Wideband Phased Arrays Using Metamaterial Absorbers,” in *14th European Conference on Antennas and Propagation, EuCAP 2020*, Vol. 3 (Institute of Electrical and Electronics Engineers Inc., 2020).

27. D. Prabhakar, P. M. Rao, and M. Satyanarayana, “Design and Performance of Resonant Spacing Linear Patch Array With Mitered Bend Feed Network for Wireless Applications,” *Indian Journal of Science and Technology* 10, no. 31 (8 2017): 1–12, https://doi.org/10.17485/ijst/2017/v10i31/92423.

28. H. L. Liu, K. L. Ford, and R. J. Langley, “Design Methodology for a Miniaturized Frequency Selective Surface Using Lumped Reactive Components,” *IEEE Transactions on Antennas and Propagation* 57, no. 9 (2009): 2732–2738, https://doi.org/10.1109/tap.2009.2027174.

29. H. P. Walker, “Sources of Intermodulation in Diode-Ring Mixers,” *Radio and Electronic Engineer* 46, no. 5 (1976): 247–255, https://doi.org/10.1049/ree.1976.0041.

30. B. Gilbert, “A Precise Four-Quadrant Multiplier With Subnanosecond Response,” *IEEE Journal of Solid-State Circuits* 3, no. 4 (1968): 365–373, https://doi.org/10.1109/jssc.1968.1049925.

31. G. Breed, “The Mathematics of Mixers: Basic Principles,” *High Frequency Electronics* (2011): 34–36.

17518792, 2026, 1, Downloaded from https://ietresearch.onlinelibrary.wiley.com/doi/10.1049/rsn2.70150 by NICE, National Institute for Health and Care Excellence, Wiley Online Library on [11/05/2026]. See the Terms and Conditions (https://onlinelibrary.wiley.com/terms-and-conditions) on Wiley Online Library for rules of use; OA articles are governed by the applicable Creative Commons License